The Ensemble Kalman Filter as a tool for estimating temperatures in the powder bed fusion process

Nathaniel Wood, Student member, Edwin Schwalbach, Andrew Gillman, Member, David J. Hoelzle, Member

Abstract-Powder Bed Fusion (PBF) is a type of additive manufacturing process that builds parts out of metal powder in a layerwise fashion. Quality control (QC) remains an unsolved problem for PBF. Data-driven models of PBF are expensive to train and maintain, in terms of materials and machine time, because they are sensitive to changes in processing conditions. The length and time scale discrepancies of the process make physics-based modeling impractical to implement. We propose monitoring PBF with an Ensemble Kalman Filter (EnKF). The EnKF combines the computational efficiency of datadriven models with the flexibility of physics-based models, while mitigating the flaws of either method. We validate EnKF performance for linear process models, using finite element method data in place of measured experimental data. We show that the EnKF can reduce the error signal 2-norm and ∞ -norm relative to the open loop model by as much as 75%.

I. INTRODUCTION

Metal Powder Bed Fusion (PBF) is a type of additive manufacturing (AM) process that builds parts out of a bed of metal powder in a layer-by-layer fashion. The PBF build process is implemented in two ways: using an electron beam as a heat source (E-PBF, Fig. 1a), or a laser as a heat source (L-PBF, Fig. 1b). Both implementations operate in a three stage cycle: (i) spread a layer of metal powder over the platform base plate or a layer of previously-fused powder, (ii) run the localized heat source overtop the powder, fusing a 2D pattern of solid material within the powder, and (iii) index the base plate in the -z direction to accommodate a fresh layer of powder, beginning the cycle anew. PBF has greatly expanded its market share in recent years, due to the process's ability to manufacture near net-shape parts with unparalleled geometric complexity and flexibility of production while simultaneously reducing overhead costs [2], [3]. Despite the overall rapid adoption of PBF by industry, its expansion into certain markets has been limited. Such markets include rotating engine components in airplanes and other parts that feature strict quality control standards. The reluctance to

Final manuscript submitted on March 5, 2021. This work was supported by AFRL award C.N. RX9-OSU-20-5-AFRL2, and by the member organizations of the Smart Vehicle Concepts Center, a Phase III National Science Foundation Industry-University Cooperative Research Center (www.SmartVehicleCenter.org) under grant NSF IIP 1738723.

Nathaniel Wood is with the Department of Mechanical and Aerospace Engineering at the Ohio State University, Columbus, OH, 43210 USA (email: wood.863@osu.edu).

Edwin Schwalbach is with the Air Force Research Laboratory, Dayton, OH, 45433-5519 USA (email: edwin.schwalbach@us.af.mil)

Andrew Gillman is with the Air Force Research Laboratory, Dayton, OH, 45433-5519 USA (email: andrew.gillman.2@us.af.mil)

David J. Hoelzle is with the Department of Mechanical and Aerospace Engineering at the Ohio State University, Columbus, OH, 43210 USA (phone: +1 (614) 688-2942; email: hoelzle.1@osu.edu).

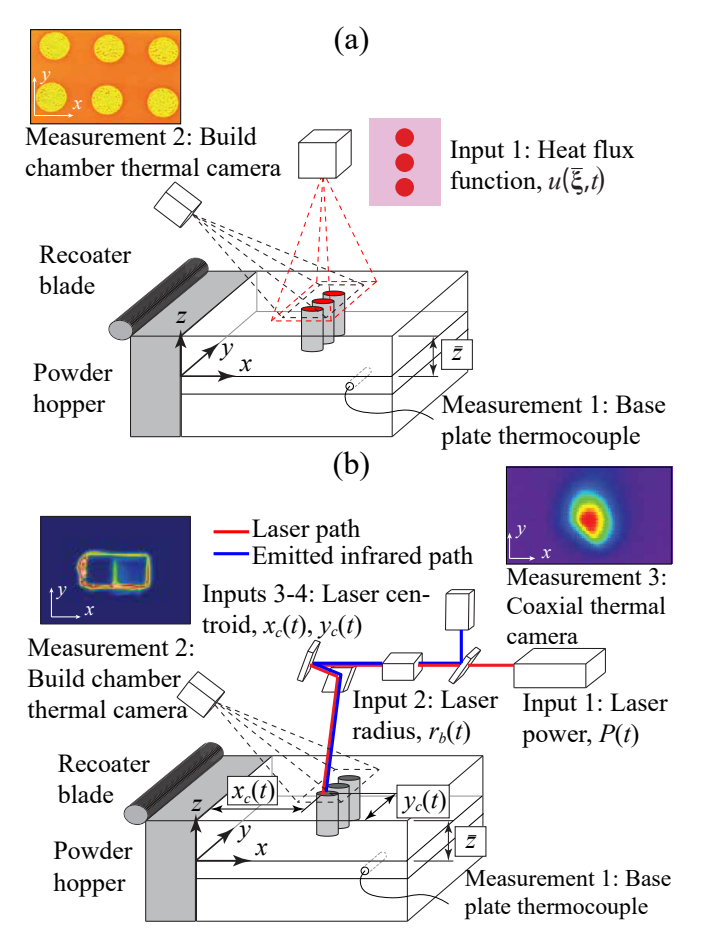


Fig. 1. System schematic of Powder bed fusion (PBF) additive manufacturing. (a) Input and output channels for E-PBF. Measurement 2 screenshot reproduced from [1] with permission from The Minerals, Metals, and Materials Society. (b) Input and output channels for L-PBF and E-PBF with a slow raster speed.

adopt PBF in these sectors stems from the fact that parts made with PBF suffer from characteristic flaws, including irregular microstructures (material property anisotropy) [3]–[7], porosity [6], [8], [9], and residual stresses [10]–[12]. These flaws typically exist in PBF-produced parts due to a lack of effective quality control (QC).

Historically, PBF QC has struggled to systematically anticipate, mitigate, and control these flaws. Machine (supervised) learning algorithms for recognizing defects in-situ have been proposed [13]–[16], but these algorithms require extensive datasets to train. Furthermore, these algorithms are inflexible to changes in processing conditions, and require retraining for alterations to parameters like part material,

part geometry, production facilities, and others. Accurate, physics-based PBF process models, which could be used to predict the presence of defects, historically have been far too computationally expensive to run in-situ [17], [18].

This work applies state estimation to combine the strengths of both approaches; incorporating in-situ data to correct for errors in a computationally efficient, but simplistic process model, that does not require training data. For a twodimensional (2D) geometry, we construct linear models of the E-PBF and L-PBF processes, which are based on the Finite Element Method (FEM). By incorporating L-PBF models, we build on previous work in this subject [19]-[21]. These models are used to subject the test geometry to simulated E-PBF and L-PBF heat sources, which return predictions of the associated temperature fields. We call these models the *open loop* (OL) models. A nonlinear FEM model that uses the same physics as the linear E-PBF and L-PBF models runs alongside the linear models. This nonlinear FEM model data is our surrogate for physical system data, which we use to apply an Ensemble Kalman Filter (EnKF) to the linear E-PBF and L-PBF models. The EnKF estimates temperature fields by correcting linear model predictions to comply with the nonlinear FEM model data. The temperature fields returned by the linear models and the EnKF are compared against those returned by the nonlinear FEM model, and their accuracy relative to the nonlinear FEM model is quantified using the 2-norm and ∞-norm of the error signals. We show that applying the EnKF reduces the 2-norm of temperature field error by up to 75%, relative to that of the corresponding OL models.

II. METHODOLOGY

A. OL model construction

The OL model is the physical process model which serves as the basis for the EnKF. Derivation of these models is detailed in [21], which we now briefly summarize. Since the EnKF compensates for modeling errors, we prioritize computational efficiency over accuracy. Therefore, we approximate the thermal physics within PBF according to Fourier's Law of Conduction

$$\begin{split} \frac{\partial T}{\partial t} &= \frac{K}{c\rho} \nabla^2 T \ \forall \ \boldsymbol{\xi} \in V \\ T &= T_0 \ \forall \ \boldsymbol{\xi} \in \Lambda \\ \nabla T \cdot \hat{\mathbf{n}} &= 0 \ \forall \ \boldsymbol{\xi} \in \Gamma \\ \nabla T \cdot \hat{\mathbf{n}} &= u(\bar{\boldsymbol{\xi}}, t) \ \forall \ \bar{\boldsymbol{\xi}} \in \Omega, \end{split} \tag{1}$$

where $\boldsymbol{\xi} = [x,y,z]'$ is the spatial coordinate, t denotes time, K is the thermal conductivity, ρ is the density, c is the specific heat, Δ is the bottom surface of the part geometry (domain) V, Ω is the uppermost surface of V, $\bar{\boldsymbol{\xi}}$ represents $\boldsymbol{\xi} \in \Omega$, and Γ collects all other surfaces of V. Fig. 2 demonstrates the location of these surfaces for a simple 2D part geometry. $u(\bar{\boldsymbol{\xi}},t)$ represents the heat flux from the PBF heat source, which depends on if the system is E-PBF (Fig. 1a) or L-PBF (Fig. 1b). We discretize V into a collection of n nodes,

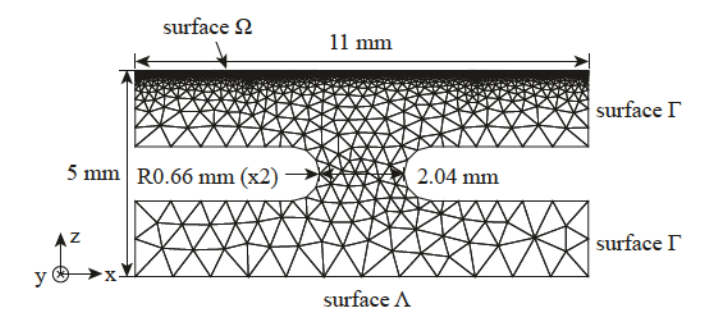


Fig. 2. FEM mesh used to test EnKF performance. The mesh consists of 4810 nodes and 8766 elements.

 $\xi_1, \xi_1, \dots, \xi_n$, connected by edges, and define the *state* vector $\mathbf{x}(t)$ as $\mathbf{x}(t) = [T(\xi_1, t), T(\xi_2, t), \dots, T(\xi_n, t)]'$. We use FEM [22] to formulate the dynamics of $\mathbf{x}(t) \in \mathbb{R}^n$ based on (1)

$$\dot{\mathbf{x}}(t) = \mathbf{A}\mathbf{x}(t) + \mathbf{r}(t, u(\bar{\xi}, t)). \tag{2}$$

A in (2) has real-valued, negative eigenvalues [21], therefore (2) has stable dynamics. Next, based on (2), we construct OL models that describe both E-PBF systems and L-PBF systems. The models differ in their input-state and output-state relationships, which are rooted in different actuation and sensing modes available to E-PBF and L-PBF. We now briefly describe the modes used to construct these models, which are detailed in [21].

1) Actuation modes: As demonstrated in Fig. 1a, the E-PBF electron beam moves so quickly overtop surface Ω that it can generate an arbitrary heat flux. This property allows us to linearize $\mathbf{r}(t,u(\bar{\boldsymbol{\xi}},t))$ by quantization in the spatial domain. We assume that the FEM mesh on surface Ω is so fine that $u(\bar{\boldsymbol{\xi}},t)$ can be reasonably approximated as constant over each element face on Ω . Fig. 2 demonstrates such a mesh. Our linearized heat input, $\mathbf{u}(t) \in \mathbb{R}^m$, collects the values of $u(\bar{\boldsymbol{\xi}},t)$ at the centroids of all such elements. In this actuation mode, the controls engineer may alter the input heat flux at any region of Ω independently of any other region. This input is distributed onto the state, $\mathbf{x}(t)$, by the input-state relationship $\mathbf{B}\mathbf{u}(t)$, where \mathbf{B} identifies which nodes in the FEM mesh belong to each element laying on Ω .

The L-PBF laser cannot move fast enough to generate an arbitrary heat flux on Ω . For L-PBF, the spatial distribution of $u(\bar{\xi},t)$ on Ω is dictated by the laser type, usually Gaussian, and is parameterized by factors like the overall laser power, beam diameter, and position. Generally, these parameters are the inputs available to the controls engineer, as noted in Fig. 1b. We generate a linear input-state relationship for L-PBF by assuming that the laser position operates on a fixed schedule that the engineer cannot control. We assume that only one laser is present, and define our input vector as $\mathbf{u}_1(t) = [P(t), r_b^2(t)]'$, where $P(t) \geq 0$ is the laser power, and $r_b^2(t) > 0$ is the squared beam radius. Using this input, we construct a Taylor series linearization

of $\mathbf{r}(t,u)$, which forms $\mathbf{r}(t,u) \approx \mathbf{B}(t)(\delta \mathbf{u}(t) + [P_0,0]')$. Here, $\mathbf{u}_0 = [P_0, r_{b0}^2]'$ is the linearization operating point, and $\delta \mathbf{u}(t) = \mathbf{u}_1(t) - \mathbf{u}_0 = [\delta P(t), \delta r_b^2(t)]$ is the deviation from the operating point. By combining terms, we arrive at the linearized input-state relationship $\mathbf{r}(t,u) \approx \mathbf{B}(t)\mathbf{u}(t)$, where $\mathbf{u}(t) = [P(t), \delta r_b^2(t)]$.

2) Measurement modes: Our E-PBF system output is Measurement 2 of Fig. 1a, which is a thermal camera that measures the temperature of surface Ω as the PBF build progresses. Thermal cameras correlate the intensity of emitted infrared light with temperature. We seek to test the feasibility of this approach, therefore, we do not factor in common hardware limitations that restrict the resolution and sampling rate of this camera. Since the camera measures all of $T(\bar{\xi},t)$, our system output, $y(t) \in \mathbb{R}^p$, simply collects the temperatures at all nodes in the FEM mesh lay on Ω . This constructs the output-state relationship y(t) = Cx(t), where C is a selection matrix of 0s and 1s that maps each component of y(t), $y_i(t)$, uniquely to a component of x(t) that corresponds to a node on surface Ω .

The L-PBF system output could be constructed from two different measurements: Measurements 2 and 3 of Fig. 1b. Measurement 2 of Fig. 1b is the same as that of Fig. 1a. Measurement 3 is a thermal camera that measures light emitted from surface Ω near the laser, which is reflected back through the optics used to control the laser, and therefore measures the temperature field of this region. We call this region near the laser, clearly shown in Measurement 3 of Fig. 1b, the PBF melt pool. In this manner, Measurement 3 "moves" with the laser beam, $x_c(t)$, and we call it a *coaxial* thermal camera. Our system output for L-PBF, $y(t) \in \mathbb{R}^p$, is the temperatures visible within the field of view (FOV) of Measurement 3. Each component of the output, $y_i(t)$, is the temperature recorded by each pixel of the camera. The output-state relationship, y(t) = C(t)x(t), interpolates the temperatures of nodes within the camera FOV into temperature values for each pixel comprising y(t). The relationship is governed by a time-varying C(t) because the selection of nodes within the camera FOV changes with time.

This procedure generates two linear OL models,

E-PBF: $\dot{\mathbf{x}}(t) = \mathbf{A}\mathbf{x}(t) + \mathbf{B}\mathbf{u}(t)$ $\mathbf{v}(t) = \mathbf{C}\mathbf{x}(t)$ (3)

L-PBF:
$$\dot{\mathbf{x}}(t) = \mathbf{A}\mathbf{x}(t) + \mathbf{B}(t)\mathbf{u}(t) \\ \mathbf{y}(t) = \mathbf{C}(t)\mathbf{x}(t).$$

Systems (3)-(4), generated using (2) and the FEM mesh of Fig. 2, feature **A** with all-distinct eigenvalues. This property, when combined with structural features of system (3) such as self-loops at every node, ξ_i , renders system (3) observable [21]. Determining conditions for the observability of system (4) is ongoing, but we can show the existence of systems (4) that are observable [21].

We discretize (2)-(4) by letting $\dot{\mathbf{x}}(t_{k+1}) = \Delta t^{-1}(\mathbf{x}(t_{k+1}) - \mathbf{x}(t_k))$, where $t_k = k\Delta t$, and $\Delta t = 1$ ms. Throughout this paper, we implement an independent realization of system (2) alongside system (3) or system (4).

The temperature predictions of system (2) are denoted as $\mathbf{x}_{FEM}(t_k)$, and the corresponding outputs as $\mathbf{y}_{FEM}(t_k)$. $\mathbf{y}_{FEM}(t_k)$ is generated from $\mathbf{x}_{FEM}(t_k)$ using the same output-state relationships as systems (3) or (4), as applicable.

B. EnKF implementation

We implement the EnKF algorithm of [23], which we summarize in Algorithm 1. Here, \mathbf{B}_k and \mathbf{C}_k represent the values of discrete-time $\mathbf{B}(t)$ and $\mathbf{C}(t)$ at $t=t_k$, as applicable. Broadly speaking, the EnKF uses an ensemble of N Kalman filters that generate simultaneous estimates of systems (3) or (4), grouped into $\mathbf{X}_k \in \mathbb{R}^{n \times N}$ and $\hat{\mathbf{X}}_k \in \mathbb{R}^{n \times N}$ of Algorithm 1. This allows the algorithm to gather sample estimates of the Kalman filter noise statistics. Using these sample statistics, the EnKF pools the ensemble estimates into a single, more accurate, state estimate. This procedure circumvents needing *a priori* knowledge of the system statistics, at the cost of greater computational burden. As indicated in Algorithm 1, physically-measured data is replaced by $\mathbf{y}_{FEM}(t_k)$ of Section II-A.

 \mathbf{V}_k of Algorithm 1 simulates taking N independent measurements of systems (3) or (4). Assuming that the engineer has access to N thermal cameras is unrealistic. We take a singular measurement, $\mathbf{y}_{FEM}(t_k)$, and construct N copies by multiplying by a row vector of ones, $\mathbf{y}_{FEM}(t_k)\mathbf{1}_{1\times N}$. To these copies, we add $\mathbf{V}_k = [\mathbf{v}_k^1,\dots,\mathbf{v}_k^N]$. Here, all $\mathbf{v}_k^i \sim \mathcal{N}(\mathbf{0},\mathbf{I})$ are independent, identically-distributed (IID) Gaussian random vectors. The addition of \mathbf{V}_k simulates the presence of N sensors of identical make, model, and calibration, that synchronously acquire noise-perturbed measurements.

 \mathbf{W}_k of Algorithm 1 simulates the independent perturbation of all N ensemble estimates by the system process noise. To help with intuition, we supply an example. Suppose that oceanic variables were estimated by N independent stations throughout a bay. Each station is subjected to random system perturbations like turbulent waters and random atmospheric effects, which are incorporated into the stations' estimates. No two estimates agree. However, the engineer can pool estimates from all stations together to get a more accurate estimation of the oceanic state. We simulate this phenomenon by perturbing the ensemble propagation of Algorithm 1, \mathbf{X}_k , by $\mathbf{W}_k = [\mathbf{w}_k^1, \dots, \mathbf{w}_k^N]$, where all $\mathbf{w}_k^i \sim \mathcal{N}(\mathbf{0}, \mathbf{I})$ are IID Gaussian random vectors.

The addition of W_k and V_k alters the error statistics between $x_{FEM}(t_k)$ and $\hat{x}_{k|k}$, and the error statistics between $y_{FEM}(t_k)$ and $\hat{y}_{k|k}$. This is because there is process noise and measurement noise associated with systems (3)-(4) that exists independently of W_k and V_k . However, since these noise sources are assumed Gaussian-distributed, the addition of Gaussian-distributed W_k and V_k keeps the noise distributions Gaussian [24]. Therefore, the inclusion of W_k and V_k does not effect the optimal nature of $\hat{x}_{k|k}$ as generated by Algorithm 1 [25].

Initialization

 $\hat{\mathbf{X}}_0 \in \mathbb{R}$, initial state ensemble $\hat{\mathbf{x}}_{0|0}$, initial state estimate

while Not end of runtime do

Predict

- $\mathbf{X}_k = \mathbf{A}\hat{\mathbf{X}}_{k-1} + \mathbf{B}_k\mathbf{u}_k\mathbf{1}_{1\times N} + \mathbf{W}_k$, propagate state ensemble
- $\cdot \mathbf{Y}_k = \mathbf{y}_{FEM}(t_k)\mathbf{1}_{1\times N} + \mathbf{V}_k$, generate measurement ensemble
- $\cdot \bar{\mathbf{x}} = N^{-1} \mathbf{X}_k \mathbf{1}_{N \times 1}, \ \bar{\mathbf{y}} = N^{-1} \mathbf{Y} \mathbf{1}_{N \times 1} \ \text{compute}$ ensemble averages

$$\begin{split} \cdot \bar{\mathbf{P}}_{k|k-1} &= \\ (N-1)^{-1} (\mathbf{X}_k - \bar{\mathbf{x}} \mathbf{1}_{1\times N}) (\mathbf{X}_k - \bar{\mathbf{x}} \mathbf{1}_{1\times N})', \\ \bar{\mathbf{R}}_{k|k-1} &= \\ (N-1)^{-1} (\mathbf{Y}_k - \bar{\mathbf{y}} \mathbf{1}_{1\times N}) (\mathbf{Y}_k - \bar{\mathbf{y}} \mathbf{1}_{1\times N})', \\ \text{compute ensemble covariances} \end{split}$$

Update

- $\cdot \tilde{\mathbf{Y}}_k = \mathbf{Y}_k \mathbf{C}_k \mathbf{X}_k$, compute ensemble innovation
- $\cdot \bar{\mathbf{S}}_{k|k-1} = \mathbf{C}_k \bar{\mathbf{P}}_{k|k-1} \mathbf{C}_k' + \bar{\mathbf{R}}_{k|k-1}, \text{ compute}$ ensemble innovation covariance
- $\cdot \mathbf{K}_k = \mathbf{\bar{P}}_{k|k-1} \mathbf{C}_k' \mathbf{\bar{S}}_{k|k-1}^\dagger$, compute Kalman gain
- $\hat{\mathbf{X}}_k = \mathbf{X}_k + \mathbf{K}_k \tilde{\mathbf{Y}}_k$, compute updated ensemble
- $\hat{\mathbf{x}}_{k|k} = N^{-1}\hat{\mathbf{X}}_k\mathbf{1}_{N\times 1}$, compute EnKF estimate
- $\cdot \hat{\mathbf{y}}_{k|k} = \mathbf{C}_k \hat{\mathbf{x}}_{k|k}$, compute Kalman output estimate

end

Algorithm 1: Ensemble Kalman Filter. † denotes pseudoinversion.

TABLE I
TEST PROCEDURES

Test	OL model	OL material set	(2) material set
i	(3)	1	1
ii	(3)	2	1
iii	(4)	1	1
iv	(4)	2	1

C. Test procedures and error metrics

EnKF performance is assessed in four different simulation-based tests. These tests return $\mathbf{x}_{FEM}(t_k)$ and $\hat{\mathbf{x}}_{k|k}$ of Section II-B, as well as the states predicted by system (3) or system (4) without the incorporation of Algorithm 1 (the OL model predictions), $\mathbf{x}_{OL}(t_k)$. Table I describes the tests. The material properties sets referenced in Table I are listed in Table II. Realizations of system (2) $(\mathbf{x}_{FEM}(t_k))$, are generated independently of systems (3)-(4) $(\mathbf{x}_{OL}(t_k))$ and $\hat{\mathbf{x}}_{k|k}$), which allows us to prescribe differing material property sets. Material set 1 represents 304 stainless steel (SS) at low temperature, and material set 2 represents 304 SS at elevated temperature [26]. Tests i and iii assess how efficiently Algorithm 1 can remove the linearization errors of systems (3)-(4), and tests ii and iv compound this error with inaccurately-known material properties.

For each test, performance is quantified with the follow-

TABLE II
MATERIAL PROPERTIES SETS

Material set	$K [\mathbf{W}^1 \mathbf{m}^{-1} \mathbf{K}^{-1}]$	$c [\mathrm{J^1 kg^{-1} K^{-1}}]$	ρ [kg ¹ m ⁻³]
1	16	500	7920
2	24	640	8070

ing error signals: $\tilde{\mathbf{x}}_{2,EnKF}(t_k) = ||\mathbf{x}_{FEM}(t_k) - \hat{\mathbf{x}}_{k|k}||_2$, $\tilde{\mathbf{x}}_{2,OL}(t_k) = ||\mathbf{x}_{FEM}(t_k) - \mathbf{x}_{OL}(t_k)||_2$, $\tilde{\mathbf{x}}_{\infty,EnKF}(t_k) = ||\mathbf{x}_{FEM}(t_k) - \hat{\mathbf{x}}_{k|k}||_{\infty}$, and $\tilde{\mathbf{x}}_{\infty,OL}(t_k) = ||\mathbf{x}_{FEM}(t_k) - \mathbf{x}_{OL}(t_k)||_{\infty}$. To compare the relative magnitude of these error signals, we also take their overall norms: $||\tilde{\mathbf{x}}_{2,EnKF}(t_k)||_2$, $||\tilde{\mathbf{x}}_{2,OL}(t_k)||_2$, $||\tilde{\mathbf{x}}_{\infty,EnKF}(t_k)||_{\infty}$, and $||\tilde{\mathbf{x}}_{\infty,OL}(t_k)||_{\infty}$.

D. Test parameters

All tests use the FEM mesh shown in Fig. 2. Surface Ω receives the system input $\mathbf{u}(t)$ and generates the output $\mathbf{y}(t)$. All nodes on surface Λ are constrained to have temperature T=0. For all tests, the initial condition is $\mathbf{x}(0)=0$, and N of Section II-B is N=50,000. All tests last 1152 time steps. For both systems, the heat input $\mathbf{u}(t)$ is based on a Gaussian-distributed linear heat source

$$u(x,t) = P(t)\sqrt{\frac{\pi}{r_b^2}} \exp\left(-\frac{(x_c(t) - x)^2}{r_b^2}\right),$$
 (5)

where $x_c(t)=0.008t$ (m), and P(t) has a 15 ms duty cycle consisting of 5 ms at 250 W, followed by 10 ms at 5 W. u(x,t) represents a L-PBF laser with specified parameters, or a particular type of E-PBF heat flux function. Systems (2)-(4) use a value of $r_b=80~\mu\mathrm{m}$, except for the realization of system (2) used in tests iii-iv. This system uses $r_b=100~\mu\mathrm{m}$, so chosen because system (4) is constructed assuming $r_{b0}=80~\mu\mathrm{m}$ (Section II-A.1), and we wish to test the influence of nonzero $\delta r_b^2(t)$ in u(t) of system (4). Recall that $\delta r_b^2(t)$ is the difference between $r_b^2(t)$, the system squared beam radius (used to realize system (2)), and the operating point, $r_{b0}^2(t)$, used to construct system (4). $\mathbf{B}(t)$ of system (4) is generated using a power operating point of $P_0=250~\mathrm{W}$, as explained in Section II-A.1.

y(t) of system (4) is constructed by simulating a coaxial thermal camera with a 3.5 mm FOV and p = 544 pixels.

III. RESULTS AND DISCUSSION

To help with reader intuition, we include representative examples of the estimated temperature fields at time step k=905 for tests ii and iv. We include $\mathbf{x}_{FEM}(t_{905})$, $\hat{\mathbf{x}}_{905|905}$, $\mathbf{y}_{FEM}(t_{905})$, and $\hat{\mathbf{y}}_{905|905}$, which are shown in Figs. 3-4. In Fig. 3 and Fig. 4a, we show the interpretation of the state, $\mathbf{x}(t_k)$, as a temperature distribution. The vertical green bars in Fig. 4a denote the limits of the coaxial thermal camera FOV, which governs the output-state relationship of system (4). Recall that the output of system (4) is the temperatures in the portion of surface Ω that lay in this FOV (the melt pool, Section II-A.2), as demonstrated in Fig. 4b.

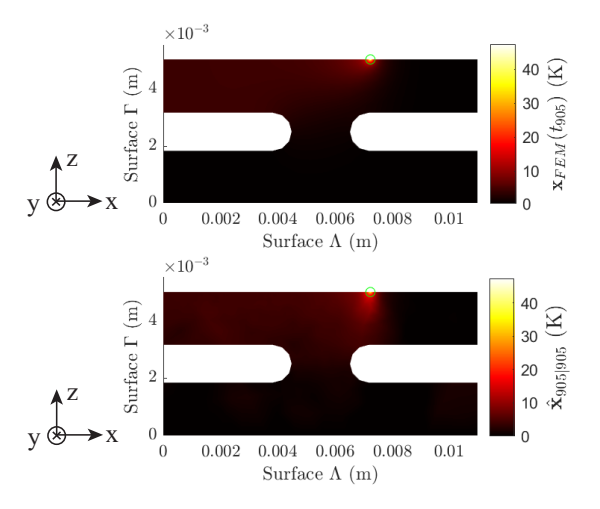


Fig. 3. Test ii, representative results from t_{905} . The green circle indicates the location of the laser.

We note that in Fig. 4b, there is good agreement between $\mathbf{y}_{FEM}(t_{905})$ and $\hat{\mathbf{y}}_{905|905}$. Fig. 5 expands this observation by plotting the error signals of Section II-C associated with each test. Qualitatively, the error 2-norm signals, $\tilde{\mathbf{x}}_2(t_k)$, assess the overall accuracy between $\hat{\mathbf{x}}_{k|k}$ or $\mathbf{x}_{OL}(t_k)$ with $\mathbf{x}_{FEM}(t_k)$, which Algorithm 1 seeks to minimize. The error ∞ -norm signals, $\tilde{\mathbf{x}}_{\infty}(t_k)$, identify the node (state component) with the maximum temperature error, and the error at this node. During our analysis, we observe that this node usually lays in the melt pool, as it is the region of $\mathbf{x}(t_k)$ with the largest temperatures.

Several important trends are noticeable in Fig. 5. With the exception of $\tilde{\mathbf{x}}_{2,EnKF}$ of test iii, Algorithm 1 produces error signals with lesser magnitude than the corresponding OL model, as quantified in Tables III-IV. In test iii, the magnitudes of $\tilde{\mathbf{x}}_{2,EnKF}(t_k)$ and $\tilde{\mathbf{x}}_{\infty,EnKF}(t_k)$ are always greater than those of $\tilde{\mathbf{x}}_{2,OL}(t_k)$ and $\tilde{\mathbf{x}}_{\infty,OL}(t_k)$, as shown in Fig. 5a and Table IV. We believe this discrepancy is tied to how test iii generates $\mathbf{x}_{FEM}(t_k)$, $\mathbf{x}_{OL}(t_k)$, and $\hat{\mathbf{x}}_{k|k}$ by applying a common material properties set to (4), thus minimizing the error between $\mathbf{x}_{FEM}(t_k)$ and $\mathbf{x}_{OL}(t_k)$. Algorithm 1 must estimate very small error quantities, which effects estimation accuracy. The value of N used in these tests, N = 50,000, may not be sufficient to overcome this deficiency. In test iv, which applies imperfect material properties knowledge to (4), Algorithm 1 successfully reduces the 2-norm and ∞ norm error signals (Table IV). We observe the same trend in tests i and ii, which considered system (3). Compared to OL error metrics (Fig. 5 and Table III), we note that the Algorithm 1-produced reductions in $\tilde{\mathbf{x}}_2(t_k)$ and $\tilde{\mathbf{x}}_{\infty}(t_k)$ are less for test i than they were in test ii. We believe this is because the error is primarily driven by a material property mismatch, not linearization error.

By comparing Tables III-IV, we observe that system (3) reduces $\tilde{\mathbf{x}}_2(t_k)$ more than system (4), and that system

- (3) reduces $\tilde{\mathbf{x}}_{\infty}(t_k)$ less than system (4). $\mathbf{y}(t_k)$ of system
- (3) measures all of surface Ω , therefore it contains more

information about the state components far afield of the melt pool than $\mathbf{y}(t_k)$ of system (4), which only measures surface Ω near the melt pool. Using more extensive measurements of the state results in superior reduction of $\tilde{\mathbf{x}}_2(t_k)$. In contrast, because $\mathbf{y}(t_k)$ of system (4) is more focused on the melt pool than $\mathbf{y}(t_k)$ of system (3), Algorithm 1 is more biased towards removing error in the melt pool. Therefore, system (4) reduces $\tilde{\mathbf{x}}_{\infty}(t_k)$ more than system (3).

Finally, we note that reduced error signal magnitudes do not imply reduction in error everywhere in V. For example, in Fig. 4a, we observe that at t = 905 ms into test iv, the melt pool (region of elevated temperatures) of $\hat{\mathbf{x}}_{k|k}$ extends overly far into the -z axis, as measured by the emulator of the true system, $\mathbf{x}_{FEM}(t_k)$. In this portion of the build, Algorithm 1 increases the error. However, by observing Fig. 5b, we note that $\tilde{\mathbf{x}}_{2,EnKF}(t_{905})$ is well beneath $\tilde{\mathbf{x}}_{2,OL}(t_{905})$. The discrepancy is due to reductions in $\tilde{\mathbf{x}}_{\infty,EnKF}(t_k)$, which means reducing the errors in the melt pool estimation, where the temperature magnitudes are the largest and the associated errors have the largest magnitude. As noted in Table IV, $||\tilde{\mathbf{x}}_{\infty,EnKF}(t_k)||_{\infty}$ is beneath $||\tilde{\mathbf{x}}_{\infty,OL}(t_k)||_{\infty}$ for test iv. Reducing the melt pool error lowers the magnitude of $\tilde{\mathbf{x}}_{2.EnKF}$ so much that it stays less than $\tilde{\mathbf{x}}_{2,OL}$, even though there are minor increases in error far afield of the melt pool. Our analysis reveals that this was not an occasional occurrence. Algorithm 1 generates an overly-deep melt pool whenever a material properties mismatch is present (test iv and test ii, Fig. 3). The presence of this phenomenon throughout test ii is especially interesting, given the large reduction in $||\tilde{\mathbf{x}}_2(t_k)||_2$ shown in Table III. We intend to minimize the error signal more uniformly far afield of the melt pool by introducing localization [27] to Algorithm 1. Minimizing this error is desirable for several reasons. For example, several defects in PBF parts are correlated with unusually-deep melt pools. Artificially-deep estimated melt pools, as shown in Fig. 3-4a, would cause a PBF QC algorithm to incorrectly flag a build for supposedly having these defects.

IV. CONCLUSIONS

This paper demonstrates the feasibility of using an Ensemble Kalman Filter (EnKF) to estimate internal temperature distributions in the PBF process. Our analysis was restricted to two-dimensional models, to reduce computational burden. We used FEM models of the PBF process instead of physically-measured data, which allowed us to directly quantify the state error. Our tests assessed EnKF estimation error for E-PBF and L-PBF systems when the assumed material properties matched the FEM simulation, and when they differed. These tests showed that the EnKF can reduce the error 2-norm with respect to the open loop (OL) model, for both E-PBF and L-PBF systems, when material properties differed. This reduction was as high as a 75% reduction in error 2-norm. When material properties matched, the L-PBF system produced an anomalous 2-norm error signal, which we attribute to inaccurate assumptions of the system statistics.

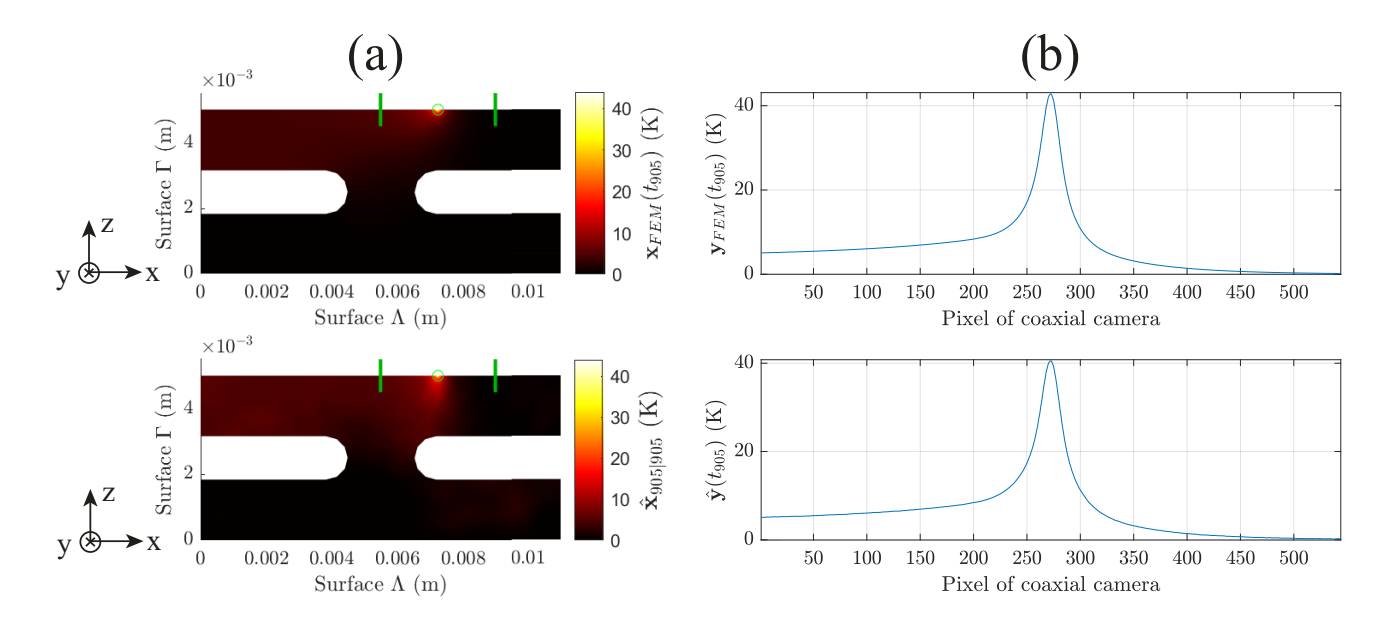


Fig. 4. Test iv, representative results from t_{905} . (a) Comparison of $\mathbf{x}_{FEM}(t_k)$ and $\hat{\mathbf{x}}_{k|k}$. The green circle indicates the location of the laser, and the green bars denote the boundary of the coaxial camera FOV. (b) Comparison of FEM output and EnKF-estimated output.

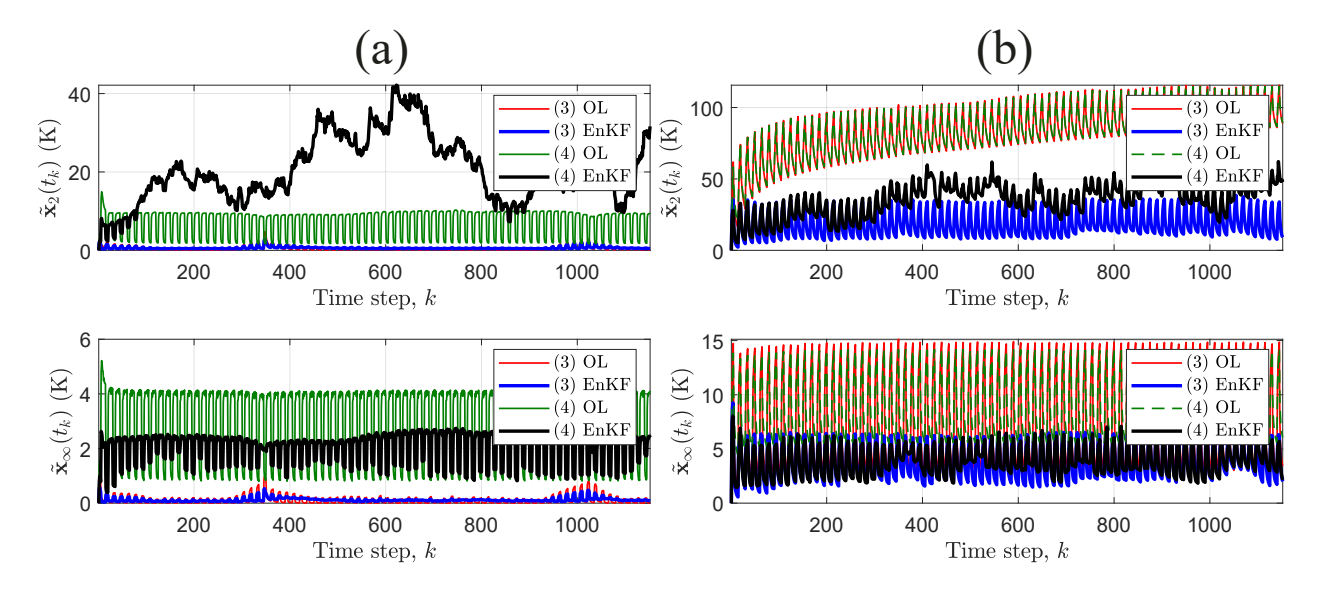


Fig. 5. Comparison of error norms for each test. Here, "EnKF" refers to Algorithm 1. (a) Tests i and iii. (b) Tests ii and iv.

TABLE III

OVERALL ERROR NORMS OF ALL TESTS FOR SYSTEM (3)

	Test i		Test ii	
	$ \tilde{\mathbf{x}}_2(t_k) _2$	$ \tilde{\mathbf{x}}_{\infty}(t_k) _{\infty}$	$ \tilde{\mathbf{x}}_2(t_k) _2$	$ \tilde{\mathbf{x}}_{\infty}(t_k) _{\infty}$
Algorithm 1	23.11	0.59	712.44	9.27
OL	25.47	0.98	2870.34	15.12
Reduction (%)	9.3	39.8	75.2	38.7

Our tests also showed that minimizing the 2-norm does not imply minimizing the error everywhere in the part geometry. We showed that the EnKF estimation error was slightly

higher than the OL model in regions far afield of the system outputs, for both E-PBF and L-PBF systems. Despite this error increase, the error 2-norm decreased due to large error

TABLE IV

OVERALL ERROR NORMS OF ALL TESTS FOR SYSTEM (4)

	Test iii		Test iv	
	$ \tilde{\mathbf{x}}_2(t_k) _2$	$ \tilde{\mathbf{x}}_{\infty}(t_k) _{\infty}$	$ \tilde{\mathbf{x}}_2(t_k) _2$	$ \tilde{\mathbf{x}}_{\infty}(t_k) _{\infty}$
Algorithm 1	753.06	2.74	1267.67	8.03
OL	264.77	5.22	2879.48	14.26
Reduction (%)	-184.4	47.5	56.0	43.7

reductions in the vicinity of the system output, where the process generated the highest temperatures. As such, the EnKF did not correct the far-afield error increase, because the objective of minimizing the 2-norm was already satisfied.

We will pursue several avenues of research in light of these results. First, encouraged by our EnKF performance with simulated data, we will implement the EnKF with experimental data [28]. We intend to incorporate localization [27] into our algorithm, to ensure that the algorithm more heavily prioritizes reducing error far afield of the system output. We also intend to assess the algorithm performance for 3D process models. This research will demonstrate algorithm efficacy under increasingly-realistic models of the PBF process, thus affirming the feasibility of this approach in more realistic contexts.

REFERENCES

- [1] S. Ridwan, J. Mireles, S. Gaytan, D. Espalin, and R. Wicker, "Automatic layerwise acquisition of thermal and geometric data of the electron beam melting process using infrared thermography," in Proceedings of the Annual International Solid Freeform Fabrication Symposium, Austin, TX, USA, 2014, pp. 343–352.
- [2] V. Bhavar, P. Kattire, V. Patil, S. Khot, K. Gujar, and R. Snigh, "A review of powder bed fusion technology of metal additive manufacturing," in 4th International conference and exhibition on additive manufacturing technologies, Banglore, India, 2014, pp. 1–2.
- [3] T. Wang, Y. Zhu, S. Zhang, and H. Wand, "Grain morphology evolution behavior of titanium alloy components during laser melting deposition additive manufacturing," *Journal of Alloys and Compounds*, vol. 632, pp. 505–513, 2015.
- [4] J. Keist and T. Palmer, "Role of geometry on properties of additively manufactured ti-6al-4v structures fabricated using laser based directed energy deposition," *Materials and Design*, vol. 106, pp. 482–494, 2016.
- [5] H. Wei, J. Elmer, and T. DebRoy, "Origin of grain orientation during solidification of an aluminum alloy," *Acta Materialia*, vol. 115, pp. 123–131, 2016.
- [6] T. Mower and M. Long, "Mechanical behavior of additive manufactured, powder-bed laser-fused materials," *Materials Science and Engineering: A*, vol. 651, pp. 198–213, 2016.
- [7] A. Yadollahi, N. Shamsaei, S. Thompson, and D. Seely, "Effects of process time interval and heat treatment on the mechanical and microstructural properties of direct laser deposited 316l stainless steel," *Materials Science and Engineering: A*, vol. 644, pp. 171–183, 2015.
- [8] P. K. Gokuldoss, S. Kolla, and J. Eckert, "Additive manufacturing processes: Selective laser melting, electron beam melting and binder jetting – selection guidelines," *Materials (Basel)*, vol. 10, no. 6, June 2017.
- [9] T. DebRoy, H. Wei, J. Zuback, T. Mukherjee, J. Elmer, J. Milewski, A. Beese, A. Wilson-Heid, A. De, and W. Zhang, "Additive manufacturing of metallic components – process, structure and properties," *Progress in Materials Science*, vol. 62, pp. 112–224, 2017.
- [10] H. Peng, D. B. Go, R. Billo, S. Gong, M. R. Shankar, B. Aboud Gatrell, J. Budzinski, P. Ostiguy, R. Attardo, C. Tomonto, J. Neidig, and D. J. Hoelzle, "Fast prediction of thermal distortion in metal powder bed fusion additive manufacturing: Part 1, a thermal

- circuit network model," *Additive Manufacturing*, vol. 22, pp. 852–868, 2018.
- [11] H. Peng, M. Ghasri-Khouzani, S. Gong, R. Attardo, P. Ostiguy, R. B. Rogge, B. Aboud Gatrell, J. Budzinski, C. Tomonto, J. Neidig, M. R. Shankar, R. Billo, D. B. Go, and D. J. Hoelzle, "Fast prediction of thermal distortion in metal powder bed fusion additive manufacturing: Part 2, a quasi-static thermo-mechanical model," *Additive Manufacturing*, vol. 22, pp. 869–882, 2018.
- [12] T. Krol, C. Seidel, J. Schilp, M. Hofmann, W. Gan, and M. Zaeh, "Verification of structural simulation results of metal-based additive manufacturing by means of neutron diffraction," *Physics Procedia*, vol. 41, pp. 849 – 857, 2013, lasers in Manufacturing (LiM 2013).
- [13] M. Cola and S. Betts, "In-situ process mapping using thermal quality signaturesTM during additive manufacturing with titanium alloy ti-6al-4v," Sigma Labs, Tech. Rep. BY6-2018-003IR Rev0, 2018.
- [14] A. Gaikwad, R. Yavari, M. Montazeri, K. Cole, L. Bian, and P. Rao, "Toward the digital twin of additive manufacturing: Integrating thermal simulations, sensing, and analytics to detect process faults," *IISE Transactions*, 2020.
- [15] Z. Yang, D. Eddy, S. Krishnamurty, and I. Grosse, "Investigating grey-box modeling for predictive analytics in smart manufacturing," in ASME IDETC/CIE 2017, 2017, pp. DETC2017–67794.
- [16] T. Mukherjee and T. DebRoy, "A digital twin for rapid qualification of 3d printed metallic components," *Applied Materials Today*, vol. 14, pp. 59–65, 2019.
- [17] S. Khairallah and A. Anderson, "Mesoscopic simulation model of selective laser melting of stainless steel powder," *Journal of Materials Processing Technology*, vol. 214, pp. 2627–2636, 2014.
- [18] P. Witherell, Y. Zhang, and V. Shapiro, "Towards thermal simulation of powder bed fusion on path level," in ASME 2019 International Design Engineering Technical Conferences and Computers and Information in Engineering Conference, Anaheim, CA, USA, August 2019.
- [19] N. Wood and D. Hoelzle, "On the feasibility of a temperature state observer for powder bed fusion additive manufacturing," in 2018 Annual American Control Conference (ACC), 2018, pp. 321–328.
- [20] ——, "seeing' the temperature inside the part during the powder bed fusion process," in *Solid Freeform Fabrication Symposium (SFF) 2019*, 2019, pp. 172–191.
- [21] —, "On the controllability and observability of temperature states in powder bed fusion," 2021, submitted to IEEE TCST.
- [22] R. D. Cook, D. S. Malkus, and M. E. Plesha, Concepts and Applications of Finite Element Analysis, 3rd ed. John Wiley and Sons, Inc., 1989.
- [23] G. Evensen, "The ensemble kalman filter: theoretical formulation and practical implementation," *Ocean Dynamics*, vol. 53, pp. 343–367, 2003.
- [24] Y. Tong, The Multivariate Normal Distribution. New York, NY: Springer-Verlag, 1990.
- [25] R. Kalman, "A new approach to linear filtering and prediction problems," *Transactions of the ASME-Journal of Basic Engineering*, vol. 82, no. Series D, pp. 35–45, 1960.
- [26] F. Cverna, Ed., Thermal Properties of Metals. Materials Park, Ohio: ASM International, 2002.
- [27] S. Greybush, E. Kalnay, T. Miyoshi, K. Ide, and B. Hunt, "Balance and ensemble kalman filter localization techniques," *Monthly Weather Review*, vol. 139, no. 2, pp. 511–522, 2011.
- [28] N. Wood, H. Mendoza, P. Boulware, and D. Hoelzle, "Interrogation of mid-build internal temperature distributions within parts being manufactured via the powder bed fusion process," in *Solid Freeform Fabrication Symposium (SFF) 2019*, 2019, pp. 1445–1481.